



**University of
Zurich**^{UZH}

**Zurich Open Repository and
Archive**

University of Zurich
University Library
Strickhofstrasse 39
CH-8057 Zurich
www.zora.uzh.ch

Year: 2023

Volumetric measurements of weak current-induced magnetic fields in the human brain at high resolution

Göksu, Cihan ; Gregersen, Fróði ; Scheffler, Klaus ; Eroğlu, Hasan H ; Heule, Rahel ; Siebner, Hartwig R ;
Hanson, Lars G ; Thielscher, Axel

DOI: <https://doi.org/10.1002/mrm.29780>

Posted at the Zurich Open Repository and Archive, University of Zurich

ZORA URL: <https://doi.org/10.5167/uzh-253839>

Journal Article

Published Version









The following work is licensed under a Creative Commons: Attribution-NonCommercial-NoDerivatives 4.0 International (CC BY-NC-ND 4.0) License.

Originally published at:

Göksu, Cihan; Gregersen, Fróði; Scheffler, Klaus; Eroğlu, Hasan H; Heule, Rahel; Siebner, Hartwig R; Hanson, Lars G; Thielscher, Axel (2023). Volumetric measurements of weak current-induced magnetic fields in the human brain at high resolution. *Magnetic Resonance in Medicine*, 90(5):1874-1888.

DOI: <https://doi.org/10.1002/mrm.29780>

Volumetric measurements of weak current-induced magnetic fields in the human brain at high resolution

Cihan Göksu^{1,2} | Fróði Gregersen^{1,3,4}  | Klaus Scheffler^{2,5}  |
 Hasan H. Eroglu^{1,3}  | Rahel Heule^{2,5}  | Hartwig R. Siebner^{1,6,7} |
 Lars G. Hanson^{1,3}  | Axel Thielscher^{1,3} 

¹Danish Research Centre for Magnetic Resonance, Center for Functional and Diagnostic Imaging and Research, Copenhagen University Hospital Amager and Hvidovre, Copenhagen, Denmark

²High-Field Magnetic Resonance Center, Max-Planck Institute for Biological Cybernetics, Tübingen, Germany

³Section for Magnetic Resonance, DTU Health Tech, Technical University of Denmark, Kgs Lyngby, Denmark

⁴Sino-Danish Center for Education and Research, Aarhus, Denmark

⁵Department of Biomedical Magnetic Resonance, University of Tübingen, Tübingen, Germany

⁶Department of Neurology, Copenhagen University Hospital Bispebjerg and Frederiksberg, Copenhagen, Denmark

⁷Faculty of Medical and Health Sciences, Institute for Clinical Medicine, University of Copenhagen, Copenhagen, Denmark

Correspondence

Axel Thielscher, Department of Health Technology, Technical University of Denmark, Ørstedes Plads, Building 349, 2800 Kgs. Lyngby, Denmark.
 Email: axthi@dtu.dk

Funding information

German Research Foundation, Grant/Award Number: DFG SCH 658/12; Lundbeck Foundation, Grant/Award Numbers: R186-2015-2138, R244-2017-196, R288-2018-236, R313-2019-622, R324-2019-1784

Abstract

Purpose: Clinical use of transcranial electrical stimulation (TES) requires accurate knowledge of the injected current distribution in the brain. MR current density imaging (MRCDI) uses measurements of the TES-induced magnetic fields to provide this information. However, sufficient sensitivity and image quality in humans in vivo has only been documented for single-slice imaging.

Methods: A recently developed, optimally spoiled, acquisition-weighted, gradient echo-based 2D-MRCDI method has now been advanced for volume coverage with densely or sparsely distributed slices: The 3D rectilinear sampling (3D-DENSE) and simultaneous multislice acquisition (SMS-SPARSE) were optimized and verified by cable-loop experiments and tested with 1-mA TES experiments for two common electrode montages.

Results: Comparisons between the volumetric methods against the 2D-MRCDI showed that relatively long acquisition times of 3D-DENSE using a single slab with six slices hindered the expected sensitivity improvement in the current-induced field measurements but improved sensitivity by 61% in the Laplacian of the field, on which some MRCDI reconstruction methods rely. Also, SMS-SPARSE acquisition of three slices, with a factor 2 CAIPIRINHA (controlled aliasing in parallel imaging results in higher acceleration) acceleration, performed best against the 2D-MRCDI with sensitivity improvements for the $\Delta B_{z,c}$ and Laplacian noise floors of 56% and 78% (baseline without current flow) as well as 43% and 55% (current injection into head). SMS-SPARSE reached a sensitivity of 67 pT for three distant slices at $2 \times 2 \times 3 \text{ mm}^3$ resolution in 10 min of total scan time, and consistently improved image quality.

Conclusion: Volumetric MRCDI measurements with high sensitivity and image quality are well suited to characterize the TES field distribution in the human brain.

KEYWORDS

3D volume acquisition, current-induced magnetic field, magnetic resonance current density imaging, simultaneous multislice acquisition, transcranial electrical stimulation

Lars G. Hanson and Axel Thielscher contributed equally to this work.

This is an open access article under the terms of the [Creative Commons Attribution-NonCommercial-NoDerivs](https://creativecommons.org/licenses/by-nc-nd/4.0/) License, which permits use and distribution in any medium, provided the original work is properly cited, the use is non-commercial and no modifications or adaptations are made.

© 2023 The Authors. *Magnetic Resonance in Medicine* published by Wiley Periodicals LLC on behalf of International Society for Magnetic Resonance in Medicine.

1 | INTRODUCTION

Low-intensity transcranial electric stimulation (TES; currents of 1–2 mA) is used widely in basic and clinical neuroscience.^{1,2} A better understanding of the current distribution induced by TES in the brain is needed for an optimized and personalized dose control that steers the currents to the intended target regions. Simulation tools based on realistic head models (e.g., SimNIBS)^{3,4} are useful in this regard, but their accuracy in estimating the TES current flows still needs to be validated by *in vivo* measurements of the TES-induced fields in humans.

MR current density imaging (MRCDI) is an advancing technique, combining TES (at 1–2 mA; 0–100 Hz) with MRI to map the induced current flow in the head. The TES currents cause a slight magnetic field change (less than a few nanotesla), and the current-induced magnetic field component $\Delta B_{z,c}$ that is parallel to the scanner field B_0 modulates the phase of the acquired MR image. These modulated phase images can then be used to determine the strength and distribution of the current-induced magnetic fields and to reconstruct the underlying current flow.^{5–14}

Initial successful MRCDI studies in phantoms, animals, and human limbs *in vivo*^{13–31} formed the basis for more recent *in vivo* measurements in human brain.^{32–36} However, accurate current flow mapping in the brain remains very challenging for several reasons: First, because the measured current-induced magnetic fields are below 1–2 nT due to safety and tolerability limits of about 1–2 mA for the TES currents,³⁷ thermal and physiological noise as well as instrumental instabilities result in low SNR. Second, the total scan time is limited by the ability of the participant to continuously lie still in the MR scanner. Finally, the availability of $\Delta B_{z,c}$ measurements targeting a small portion of the head only, such as a single 2D slice, results in the need for unrealistic assumptions for methods that reconstruct the TES current flow from the measured $\Delta B_{z,c}$.³⁸ This causes a poor reconstruction accuracy. Therefore, reconstruction algorithms can greatly benefit from highly sensitive volume measurements rather than 2D coverage.

The SNR of $\Delta B_{z,c}$ measurements directly scales with the strength of the current-induced magnetic fields and the inverse of the noise SD of $\Delta B_{z,c}$. The latter depends on the SNR of the MR magnitude image and the phase sensitivity of the used MRCDI method.⁷ Based on a thorough sensitivity analysis^{32,39} and technical advances to optimize the practical setup used for MRCDI experiments,^{40,41} we recently developed a 2D gradient echo–based MRCDI acquisition-weighted method with optimized spoiling and

SNR efficiency.⁴² Here, we extend our previous 2D-MRCDI approach⁴² in two ways to measure densely or sparsely covered brain volumes. In general, the SNR scales linearly with the voxel volume and the square root of the effective measurement time (product of number of phase-encoding lines, number of averages, and sampling time) for thermal noise and all other acquisition parameters fixed.⁴³ Simultaneous excitation of a large-volume subject to spatial encoding is therefore often preferred over consecutive slice excitation, as it increases the effective voxel measurement time. An exception is the successive excitation of multiple slices within the same TR (possibly with prolongation of TR to allow this), but earlier analysis has proven this strategy to be inefficient for gradient-echo MRCDI.^{32,39} Signal acquisition in a densely covered volume (3D-DENSE; Figure 1A) and simultaneous multislice excitation of a sparsely covered volume (SMS-SPARSE) are therefore attractive for MRCDI, even though the latter comes with a minor g-factor penalty. Indeed, in this study, initial optimization in phantom experiments (Appendix S1) confirmed the theoretically expected sensitivity advantages for magnetic field measurements of 3D-DENSE and SMS-SPARSE compared with 2D MRCDI. In practice, however, physiological noise sensitivity and imperfections may challenge the general SNR expectation for this application. The main aim of this study was therefore to validate and compare the different sequences by *in vivo* brain imaging.

The performance evaluations of tested sequences in this study were based primarily on $\Delta B_{z,c}$ field measurements, as their accuracy directly relates to the quality of current density image reconstructions based on a recently proposed technique.³⁸ In addition, we use the Laplacian of the field measurements as supplementary evaluation criteria, as it is used in conventional conductivity reconstruction strategies.²⁷ Although the main focus of this study is on the quality evaluation of the current-induced magnetic field measurements, the relevance of using multislice versus single-slice data for current density image reconstructions is also demonstrated.

2 | METHODS

2.1 | Subjects

We recruited 9 healthy volunteers with no previous histories of neurological or psychiatric disorders and performed three successive experiments. One volunteer participated in all three experiments, and 3 volunteers in Experiments 1 and 2. Five participants participated only

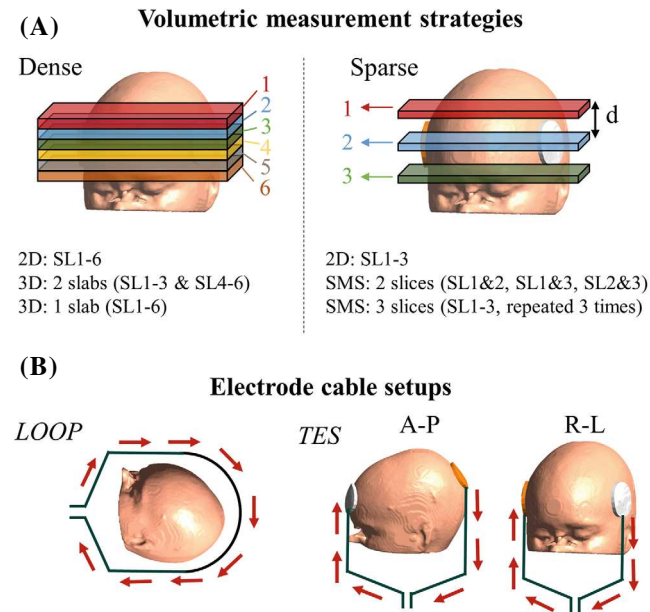


FIGURE 1 (A) Volumetric approaches for MR current density imaging (MRCDI) measurements. A volume consisting of either densely or sparsely distributed slices is selected as the imaging region. Left: For the dense acquisition, three different strategies are compared: 2D, each slice is separately measured using the 2D benchmark method; 3D–2 slabs, two imaging slabs each consisting of three slices (SL1–3 and SL4–6) are measured; and 3D–1 slab, one single slab consisting of all six slices (SL1–6) is measured. Right: For the sparse acquisition, three different strategies are compared: 2D, each slice is measured using our prior single-slice method⁴²; SMS–2 slices, three separate measurements are performed to simultaneously acquire slice pairs (SL1&2, SL1&3, and SL2&3) by simple averaging; and SMS–3 slices, all three slices SL1–3 are simultaneously measured, and this measurement is repeated 3 times to maximize SNR in the allocated scan time. (B) Similar to our prior study,⁴² two different setups are used. In the LOOP-SETUP, the current flows in a wire loop around the head. The TES-SETUP injects currents in the head either in right–left (R–L) or anterior–posterior (A–P) direction using two scalp electrodes. We used ± 2 mA baseline-to-peak currents (4 mA peak-to-peak) for the experiments using the LOOP-SETUP and ± 1 mA for the TES-SETUP (2 mA peak-to-peak). The choice of ± 2 mA for the LOOP-SETUP enabled direct comparison to results of a prior study.⁴² In particular, in that study, it increased the sensitivity of the tests to imperfections in the MR acquisitions and helped us to demonstrate errors due to imperfect spoiling that would have otherwise gone unnoticed at a lower current strength (Figure 3 in Ref. 42). We therefore kept a strength of ± 2 mA also here. TES, transcranial electrical stimulation.

in a single experiment (i.e., 1 in Experiment 1, 1 in Experiment 2, and 3 in Experiment 3). Written informed consent was obtained from all participants before the experiments. Participants were screened for any contraindication against TES and MRI. The human experimental protocols used in this study complied with the Helsinki Declaration on Human Experimentation and were approved by

the ethics committees of the medical faculty of the University of Tübingen, Germany, and the Capital Region of Denmark.

2.2 | Measuring current-induced magnetic fields

We used an optimally spoiled, multi-echo gradient echo–based MRI pulse sequence (Figure S1) and TES to create two steady-state magnetization states that are modulated by positive (+) and negative (–) current-induced magnetic fields (see Göksu et al.^{32,42} for methodological details). We used the steady-state MR signals acquired for each echo to calculate current-induced fields $\Delta B_{z,c}$ (the “z” direction is chosen along the static field direction, and “c” denotes current) from phase difference images $\angle M_n^+ - \angle M_n^- = 2\gamma \Delta B_{z,c} T_E(n)$, where γ is the proton’s gyromagnetic ratio and $T_E(n)$ is the TE of echo n . Finally, each of the calculated $\Delta B_{z,c}^n$ images were systematically weighted and combined to minimize the noise sensitivity of the combined $\Delta B_{z,c}$ image.^{32,39,42,44} We corrected the combined $\Delta B_{z,c}$ images for stray magnetic fields induced by cable currents.^{41,42}

2.3 | Volume measurements

We selected a volume consisting of either densely or sparsely placed slices (Figure 1). First, we used our prior 2D approach⁴² using separate $\Delta B_{z,c}$ measurements for each of the slices. This constituted a benchmark for testing our suggested volume measurement approaches (3D-DENSE and SMS-SPARSE): 3D-DENSE used a larger excitation volume and a second phase-encoding table (providing “slices”) for 3D k-space coverage. We used acquisition weighting in both phase-encoding directions to SNR-efficiently improve the point-spread function. These features, however, entail prolonged acquisition time and can therefore exacerbate the influences of physiological noise, which may cost sensitivity in human in vivo experiments.⁴³ Our SMS-SPARSE approach used multiband RF pulses with a CAIPIRINHA (controlled aliasing in parallel imaging results in higher acceleration) excitation scheme.⁴⁵ The multiband pulses used a systematically varying phase-cycling scheme for each of the slices to obtain a superimposed image containing each slice measurements with a controlled FOV shift, such as FOV/2 for an acceleration factor of $R=2$ (Figure S1). The superimposed image can then be unfolded using a “sensitivity encoding” (SENSE) reconstruction.⁴⁶ We obtained the required coil sensitivity maps by comparing single-element recordings to “sum-of-squares”

reconstruction of the benchmark 2D measurement. We used Tikhonov regularization in the SENSE reconstruction for the experiments with high acceleration factors $R > 2$ to maximize SNR.⁴⁷

2.4 | Measurement procedures and MRCDI experiments

Experiments 1 and 2 were conducted in the high-field MR department of the Max-Planck Institute for Biological Cybernetics and Experiment 3 was in the Danish Research Centre for Magnetic Resonance. All experiments were performed in 3T MR scanners (MAGNETOM Prisma; SIEMENS Healthcare) equipped with 64-channel head coils. The MR signals from each channel were combined using an adaptive-combine algorithm.⁴⁸

TES currents generated by an electric stimulation device (DC-STIMULATOR MR; NeuroCare Group) were injected via electrodes and cables that are made of low-conductivity silicone rubber (29.4 S/m) and optimized for MRCDI.⁴⁰ Two different setups (Figure 1B) were used in the experiments. In the LOOP-SETUP, the generated currents (± 2 mA) were flowing in a cable loop placed around the head. In the TES-SETUP, the generated currents (± 1 mA) were injected into the head via round scalp electrodes in the right-left (R-L) or anterior-posterior (A-P) direction. The LOOP-SETUP experiments also included control measurements without current injection to observe noise floors.

The study consisted of three successive experiments measuring the human brain in vivo:

1. We directly compared the sensitivity of 3D-DENSE with the benchmark 2D approach using the LOOP-SETUP for a densely covered volume.
2. We directly compared the sensitivity of SMS-SPARSE with the benchmark 2D approach using the LOOP-SETUP for a sparsely covered volume.
3. We tested our best performing volumetric approach against the benchmark 2D method using TES current injections for the two electrode montages: A-P and R-L. The measurements with the A-P montage were repeated over multiple subjects to make a direct comparison in terms of field-measurement sensitivity, reproducibility, and consistency.

In all studies, acquisition weighting was used to ensure an SNR-efficient point-spread function improvement.^{49,50} In 2D and SMS-SPARSE experiments, the k-space data were acquired in about a 1.6-times broader window and filtered with a Hanning window $h(k_{pe}) \sim 1 + \cos(2\pi k_{pe} \Delta_{pe} / \beta_w)$, where $\beta_w = 1.6$ determines the width

of the filter in both the phase-encoding and readout directions. In 3D-DENSE experiments, we extended the used filter in the second phase-encoding direction $h(k_{pe1}, k_{pe2}) \sim (1 + \cos(2\pi k_{pe1} \Delta_{pe1} / \beta_{w1}))(1 + \cos(2\pi k_{pe2} \Delta_{pe2} / \beta_{w2}))$, where $\beta_{w2} = 2$.⁵¹ The number of measurements was modified systematically (using maximum number of repetitions in the k-space center) to match the applied filter in the phase-encoding direction, which ensured a near-flat noise power spectrum after filtering (similar to Figure 2A in our previous study⁴²).

We used the first echo as a navigator as in our previous study⁴² to assess the quality of the measurements. No unexpected signal changes were observed; thus, none of the measurements were discarded.

Before the human in vivo experiments, the sensitivity and image quality of the two measurement approaches were optimized in pilot experiments in phantoms (Supporting Information Part B). Briefly, we tested various numbers of simultaneously acquired slices, interslice gaps, and different acquisition-weighting schemes. The optimized approaches were then further assessed in the in vivo Experiments 1 and 2 with the LOOP-SETUP. Finally, the most sensitive volumetric approach was tested with the TES-SETUP in Experiment 3.

2.5 | Sensitivity and image quality comparison

2.5.1 | Experiment 1: 3D-DENSE volume coverage versus 2D benchmark

We used the LOOP-SETUP (Figure 1) to compare the sensitivity and accuracy of our 3D volume acquisition approach against benchmark 2D measurements. Imaging parameters were FOV = 224×183 mm², tip angle $\alpha = 30^\circ$, TE = [6.5, 15.1, 23.7, 32.3, 40.9, 49.5, 58.1, 66.7] ms, TR = 80 ms, and an imaging matrix of 176×144 . We compared three different strategies to cover an 18-mm-thick volume (Figure 1). First, we acquired six separate single-slice 2D measurements. Second, we divided the volume into two slabs and performed 3D-DENSE measurements for each of the slabs (SL1-3 and SL4-6). Finally, we performed 3D-DENSE measurement to the entire volume as a single slab (SL1-6). For each of the strategies, the maximum number of measurements (the k-space center was acquired with a number of repetitions of 6) was used to maximize SNR under the total scan time constraint of 10 min. In each of the strategies, the actual slice resolution was kept at about $\Delta z = 3$ mm.

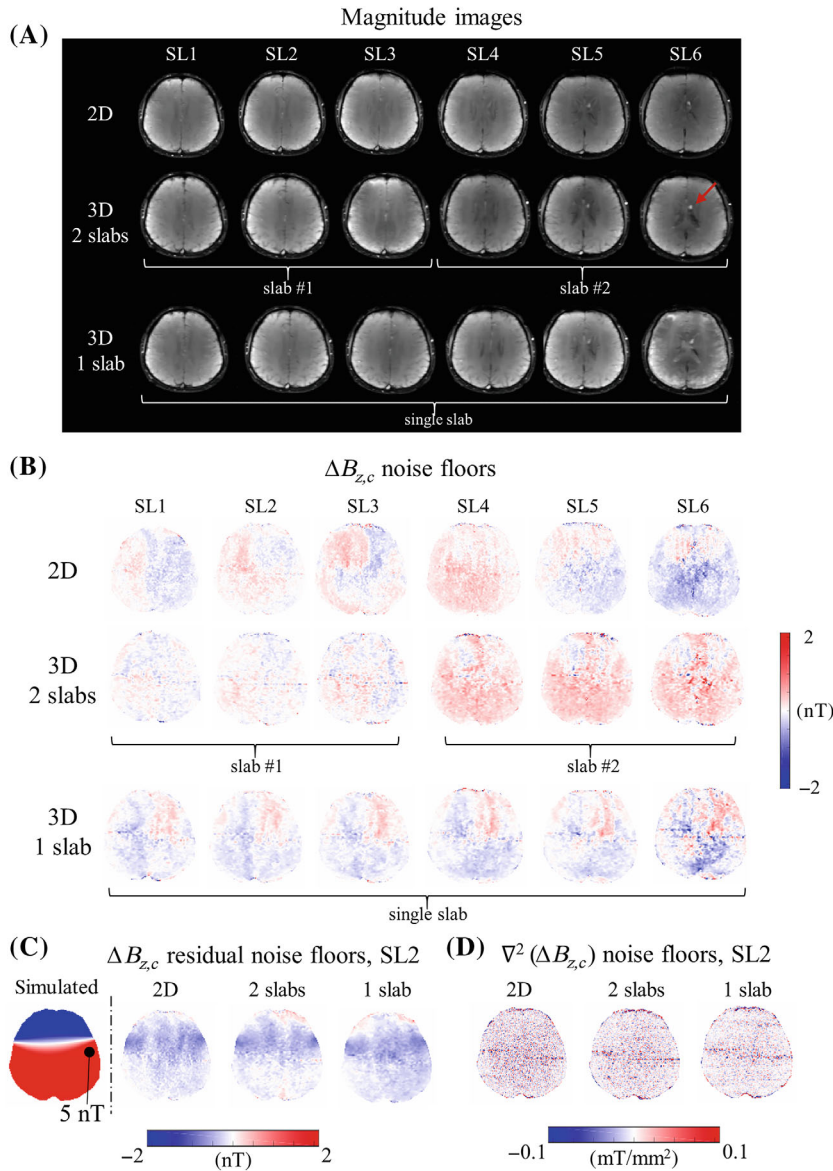


FIGURE 2 Experiment 1. Human in vivo experiments of the first subject for comparison of the 3D-DENSE approach against 2D acquisitions. (A) Apart from the image distortions in the 3D-DENSE measurements of the outer slices, the images are of good quality. Pulsation-induced artifacts are observed for all methods as indicated by a red arrow. Interestingly, 3D-DENSE technique increased the sulcus-brain tissue contrast compared with 2D, presumably because of different sensitivities to CSF flow. (B) $\Delta B_{z,c}$ noise floors for measurements without current flow. The noise floor varies significantly between measurements. Each 2D measurement and 3D slab acquisition exhibits its own, distinctive low-frequency noise pattern. (C) Comparison between residual noise floors, obtained after subtracting the simulated fields from the measurements, for current flow through the cable loop show similar spatial distributions for each technique, suggesting that intracranial head or cable motion and inaccurate cable-current correction are now the main noise sources. The simulated field is shown for comparison, and peaks at 5 nT (peak position indicated by the black dot). (D) Laplacian noise floors without current shown for SL2 demonstrate that 3D-DENSE measurements with one single-slab acquisition outperforms all other strategies. A horizontal line artifact is observed in each of the Laplacian images.

2.5.2 | Experiment 2: SMS-SPARSE volume coverage versus 2D benchmark (LOOP-SETUP)

We used the LOOP-SETUP (Figure 1) and selected a volume that consisted of three distant slices to compare the sensitivity and accuracy of SMS-SPARSE against the benchmark 2D approach. Imaging parameters were $FOV = 224 \times 183 \text{ mm}^2$, tip angle $\alpha = 30^\circ$, $TE = [6.5, 15.1, 23.7, 32.3, 40.9, 49.5, 58.1, 66.7] \text{ ms}$, $TR = 80 \text{ ms}$, and an imaging matrix of 176×144 . We compared three different strategies to cover a volume of three slices that are selected 2.5 cm apart from each other (Figure 1). First, we acquired three separate 2D measurements for each of the slices (SL1-3). Second, we used an SMS acquisition strategy⁵²⁻⁵⁴ with a set of three separate measurements to simultaneously measure each two-slice combination

(SL1&2, SL1&3, and SL2&3). In each measurement, slices were acquired with a half-FOV shift and a CAIPIRINHA acceleration factor of $R=2$. This set of measurements was then used to calculate the combined field for each of the slices (SL1, SL2, and SL3) via simple averaging. Finally, we used a similar SMS strategy to measure all three slices simultaneously (SL1-3). We acquired the center slice shifted half the FOV from the outer ones^{52,53} with $R=2$. We repeated the measurement 3 times to match the total acquisition time with the first two strategies and calculated the combined $\Delta B_{z,c}$ fields.

For each of the strategies, the maximum number of measurements (the k-space center was acquired with a number of repetitions [16]) was used to maximize SNR under the total scan time constraint of 10 min. The actual slice resolution was kept around $\Delta z = 3 \text{ mm}$.

2.5.3 | Experiment 3: SMS-SPARSE volume coverage versus 2D benchmark (TES-SETUP)

This experiment used 1-mA TES injections (Figure 1) to compare $\Delta B_{z,c}$ field measurements with the best-performing SMS-SPARSE acquisition, as determined in the prior Experiment 2, against the 2D benchmark. Similar to Experiment 2, we first acquired three separate 2D measurements for each of the slices and then used SMS-SPARSE measurements of all three slices simultaneously. The sequence parameters and calculation of the combined $\Delta B_{z,c}$ fields were identical to the ones in Experiment 2. The approximate acquisition time was 10 min for each strategy.

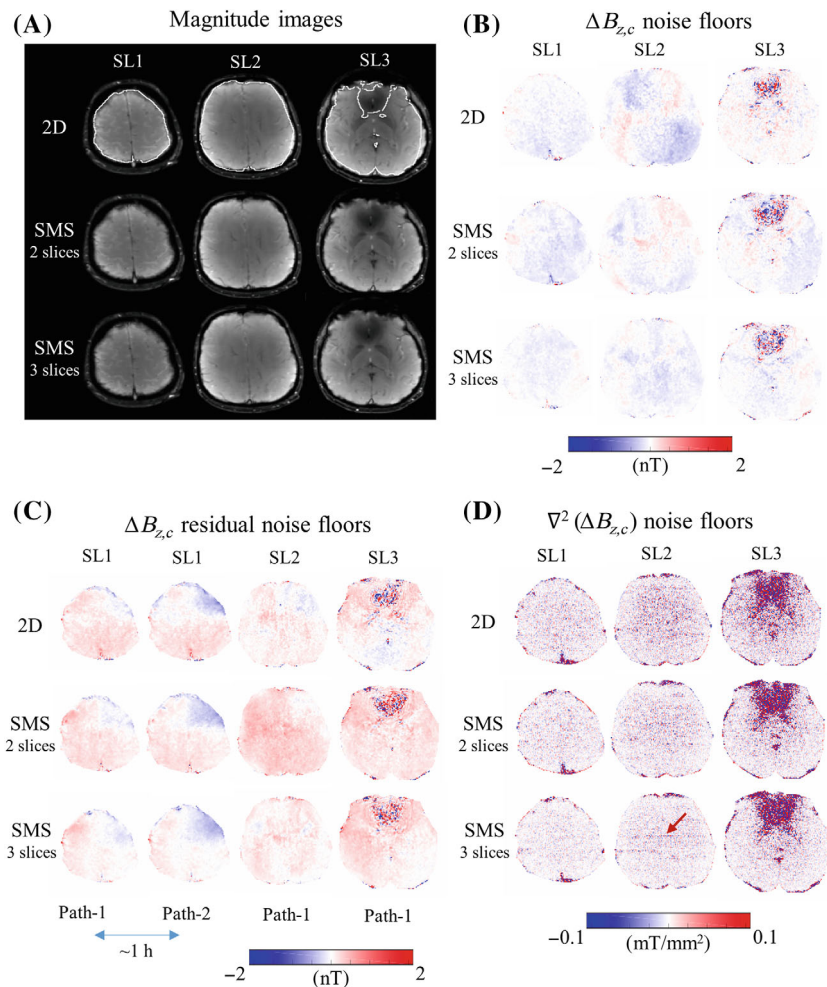
First, in 1 participant, both acquisition strategies were repeated 3 times in the same scanning session to assess the reproducibility of the results and to calculate a SD map. This was done for both electrode montages, R-L and A-P. In addition, to provide sufficient data for a robust quantitative comparison between the two strategies, the protocols were repeated 2 more times for the A-P electrode montage in subsequent scanning sessions for the same participant.

Finally, we performed $\Delta B_{z,c}$ field measurements using the A-P montage in 3 additional subjects to confirm the consistency of the observed differences between the two acquisition strategies across subjects (no repetition, 10 min per strategy).

2.6 | Noise floor measurements and cable current-induced field calculations in the $\Delta B_{z,c}$ images

We performed control measurements without current flow to measure the $\Delta B_{z,c}$ noise floor in Experiments 1 and 2. The noise floor was defined as the standard deviation of the $\Delta B_{z,c}$ measurements, referred to here as $\sigma_{\Delta B_{z,c}}$. The measurements were first masked with a T_2^* mask (20-ms threshold) to avoid regions with low signal intensity, especially in the later echoes, leading to excessive noise in the $\Delta B_{z,c}$ measurements. The T_2^* mask is indicated with a white line in the top row in Figure 3A. We used a Wilcoxon signed-rank test to assess statistical difference between the new methods (3D-DENSE and SMS-SPARSE)

FIGURE 3 Experiment 2. Human in vivo experiments of the first subject for comparison of the simultaneous multislice (SMS)-SPARSE approach against 2D acquisitions. (A) The MR magnitude images are artifact-free and of good quality. The T_2^* mask is outlined in the top row as a white line. (B) Both SMS strategies clearly improve the $\Delta B_{z,c}$ noise floors and image quality for measurements without current flow, with SMS of three slices performing slightly better. (C) Residual $\Delta B_{z,c}$ noise floors for measurements with current flow, calculated for two cable paths reconstructed from PETRA measurements performed just before and after MR current density imaging (MRCDI), respectively. The differences between the residuals based on Path 1 and Path 2 are higher than the $\Delta B_{z,c}$ noise floors of the measurements without current flow. This highlights the importance of minimizing intrascan head or cable motion and inaccuracies in the cable-current correction. (D) The sensitivity improvement provided by SMS acquisition of three slices is apparent in the Laplacian noise floors. Similar to the 3D-DENSE measurements, a subtle horizontal line artifact is observed in the Laplacian images, indicated by a red arrow.



and the 2D benchmark. The sensitivity of a measurement was defined as $1/\sigma_{\Delta B_{z,c}}$. Relative sensitivity differences were calculated as $(1/\sigma_{\Delta B_{z,c_new}} - 1/\sigma_{\Delta B_{z,c_old}})/(1/\sigma_{\Delta B_{z,c_old}})$, where $\sigma_{\Delta B_{z,c_new}}$ refers to the 3D-DENSE or SMS-SPARSE results, and $\sigma_{\Delta B_{z,c_old}}$ to the 2D benchmark. The accuracy of the SD estimates was initially validated in the phantom experiments by direct comparison with theoretically calculated SDs obtained from the MR magnitude SNR (see Appendix S1⁴² for the details).

After observing significant low-frequency noise in the experiments,^{32,42} we also performed similar noise floor calculations for the Laplacian of $\Delta B_{z,c}$, as the Laplacian is used in previously published methods for calculating the brain-tissue conductivities.²⁹ We neglected the second-order partial derivatives with respect to the B_0 direction (z) in the Laplacian calculations.

In our previous study,⁴² the control measurements for both LOOP-SETUP and TES-SETUP demonstrated similar noise floors. Thus, we performed only the experiments with TES injections in Experiment 3 here.

We also performed a noise floor analysis for the LOOP-SETUP experiments with currents flowing in a cable loop. Before each experiment, a 3D high-resolution structural scan (pointwise encoding time reduction with radial acquisition [PETRA])⁵⁵ was performed to delineate the cable paths as in our previous studies.^{32,41,42} The cable paths were used to calculate the expected $\Delta B_{z,c}$ fields using the Biot-Savart law. The differences between measured and simulated $\Delta B_{z,c}$ fields (residuals that are ideally zero) were calculated and compared with the control measurements. PETRA scans were also repeated at the end of each of the experiments in Experiment 2 to check the impact of possible cable or head movement within the session. For Experiment 3, the delineated cable paths up until the center of the scalp electrodes were used to simulate and correct for the stray magnetic fields caused by the cable currents similar to Göksu et al.⁴²

2.7 | Estimation of current density images

We used our previously introduced method³⁸ that reconstructs the induced current density by optimizing the ohmic conductivities of personalized volume conductor models of the head based on the measured $\Delta B_{z,c}$ fields. In particular, we evaluated the importance of an improved volume coverage for the stability of the reconstructed current densities. Initially, we used T_1 -weighted and T_2 -weighted structural scans to create volume conductor models of the subjects' head with CHARM³ implemented in SimNIBS.⁴ We then simulated the current density and the current-induced magnetic fields using the

finite-element method in SimNIBS, thereby optimizing the ohmic conductivities of the volume conductor models to minimize the difference between simulated and measured magnetic fields. This was done for the A-P electrode montage used with the 4 subjects in Experiment 3 with injected currents. For each subject, three single-slice measurements (~ 10 min per slice) as well as three repetitions of all slices using SMS (~ 10 min per repetition) were used.

Five variable conductivities were optimized by minimizing the difference between simulated and measured magnetic fields. The variable conductivities and their boundaries were gray matter [0.1–0.6 S/m], white matter [0.1–0.4 S/m], scalp [0.2–1 S/m], skull [0.003–0.04 S/m], and cortical CSF [0.2–1.4 S/m]. Ventricular CSF was given a constant value of 1.79 S/m. Because different sets of conductivities can give rise to approximately the same current density and current-induced magnetic field (discussed in more detail in Eroglu et al.³⁸), the current density was used as an error metric instead of the conductivities. Additionally, because the ground-truth current density is unknown, we created a reference current density per subject by performing the conductivity optimization in which the average of all SMS measurements was used as the measured magnetic field. The simulated current density with the obtained conductivities was then used as the reference current density. The reference is thus created from the best SNR and volume coverage in our data set. We then tested the error in the current density compared with the reference after conductivity optimization (i) for the three sets of SMS individually (sacrificing SNR, but not coverage) and (ii) the three single-slice measurements (keeping SNR but sacrificing coverage). Each SMS measurement was time-matched to the measurement of one single slice (~ 10 min).

3 | RESULTS

See Appendix S1 for the phantom experiments and their results that laid the foundation for the human experiments.

3.1 | Subject sensations

In accordance with previous TES-MRI studies (e.g., Refs. 32–34,42), all subjects reported only the commonly known and easily tolerable side effects of TES: phosphenes and slight tingling sensations near the electrodes that disappeared shortly after the stimulation onset.³⁷ None of the subjects reported any burning sensation, nor any other discomfort due to the stimulation.

3.2 | Sensitivity and image-quality comparison

3.2.1 | Experiment 1: 3D-DENSE volume coverage versus 2D benchmark

Results of the first subject are shown in Figure 2 to illustrate the two 3D-DENSE volume acquisition strategies (using one or two slabs) and compared with the 2D benchmark. The results for the 4 remaining subjects can be found in Figures S2–S5. No severe artifacts are observed in the magnitude images of the 2D acquisition, but significant distortions are observed in the outer slices for the 3D-DENSE acquisitions with both one and two slabs (Figure 2A). In addition, an artifact resembling CSF pulsation is clearly observed near the ventricles in the 3D-DENSE measurements, whereas it is not as strong in the 2D acquisitions. The SNR of the magnitude images was significantly improved only for the two-slab 3D measurement, but not for the one-slab measurement (Table 1).

The $\Delta B_{z,c}$ noise floors (both without current flow and residual noise floors with current flow) were not improved in any of the tested cases for the 3D-DENSE acquisition compared with the 2D benchmark (Table 1, Figure 2B,C), but rather got significantly worse in some cases. We

conclude that the improvement to the $\Delta B_{z,c}$ noise floors in the 3D-DENSE measurements is compromised by increased sensitivity to subject motion and scanner instabilities. Interestingly, the Laplacian noise floors of the 3D-DENSE strategy with one slab acquisition performed better than 2D (61% average sensitivity increase; Figure 2D). The improvement was consistently observed in each of the 5 participants and was statistically significant. This indicates that the 3D-DENSE strategy with one slab acquisition results in the lowest level of spatial high-frequency noise, in line with a reduced contribution of thermal noise to the measured signal in 3D versus 2D acquisitions expected from theory.

In each noise floor image, a horizontal line artifact is observed that is consistent with an in-line blood vessel. Overall, this artifact is observed in approximately half of the Laplacian noise images of the 5 participants for 3D-DENSE acquisition.

3.2.2 | Experiment 2: SMS-SPARSE volume coverage versus 2D benchmark (LOOP-SETUP)

Results of the first subject are shown in Figure 3 to illustrate the two SMS-SPARSE acquisition strategies and

TABLE 1 Comparison of 2D and 3D-DENSE approaches.

Noise floor measurements, Loop-SETUP: 2 mA for the residual $\Delta B_{z,c}$ and 0 mA otherwise								
SNR magnitude	SL1	SL2	SL3	SL4	SL5	SL6	Avg	Wilcoxon test
2D	712	701	659	561	615	603	642	
2 slabs	643	728	460	459	480	366	523	$p < 0.001$
1 slab	632	713	723	669	602	401	623	$p > 0.1$
SD of $\Delta B_{z,c}$ (pT)								
2D	155	196	191	153	196	254	190	
2 slabs	163	195	216	209	253	262	216	$p = 0.01$
1 slab	157	158	156	157	149	293	178	$p > 0.1$
SD of residual $\Delta B_{z,c}$ (pT)								
2D	182	233	215	188	188	283	215	
2 slabs	185	196	281	246	259	294	243	$p = 0.004$
1 slab	194	211	190	173	167	380	219	$p > 0.1$
SD of $\nabla^2(\Delta B_{z,c})$ ($\mu\text{T}/\text{mm}^2$)								
2D	34.0	29.9	31.8	33.6	50.3	95.0	45.8	
2 slabs	24.8	25.8	37.6	35.8	65.9	57.8	41.3	$p > 0.1$
1 slab	25.1	19.4	20.7	22.1	21.0	63.0	28.5	$p < 0.001$

Note: Comparison of 2D and 3D-DENSE approaches in terms of SNR calculated in the MR magnitude images, and SDs calculated in the noise floor measurements: $\Delta B_{z,c}$ (measurements without current) in pT, residual $\Delta B_{z,c}$ (measurements with current and after cable correction) in pT, and the Laplacian $\nabla^2(\Delta B_{z,c})$ in $\mu\text{T}/\text{mm}^2$. Each calculation is given as an average across 5 subjects. All data were first masked with T_2^* masks (see Table S1 for homogenous region of interest and theoretically calculated SNR-based noise floor results). The Laplacian noise floors $\nabla^2(\Delta B_{z,c})$ were calculated by neglecting the variations in the slice direction. The Wilcoxon signed-rank test was used to test for significance.

TABLE 2 Comparison of 2D and SMS-SPARSE approaches.

Noise floor measurements, Loop-SETUP: 2 mA for the residual $\Delta B_{z,c}$ and 0 mA otherwise											
SNR magnitude	SL1	SL2	SL3	Avg	Wilcoxon test	SD of $\Delta B_{z,c}$					
						(pT)	SL1	SL2	SL3	Avg	Wilcoxon test
2D	1173	878	658	903		2D	93	137	191	140	
SMS 2 slices	1392	1009	938	1113	$p < 0.001$	SMS 2 slices	82	99	169	116	$p = 0.03$
SMS 3 slices	1895	1261	1011	1389	$p < 0.001$	SMS 3 slices	59	91	120	90	$p < 0.001$
Std of residual $\Delta B_{z,c}$ (pT)						SD of $\nabla^2 (\Delta B_{z,c})$ ($\mu\text{T}/\text{mm}^2$)					
2D	157	142	261	187		2D	18.8	32.3	39.9	30.3	
SMS 2 slices	140	118	204	154	$p = 0.015$	SMS 2 slices	14.3	17.6	30.5	20.8	$p < 0.001$
SMS 3 slices	152	120	185	153	$p = 0.09$	SMS 3 slices	11.7	14.6	24.6	17.0	$p < 0.001$
TES measurements, TES-SETUP: 1 mA current injections in A-P direction											
SD of $\Delta B_{z,c}$ (pT)	SL1	SL2	SL3	Avg	Wilcoxon test	SD of $\nabla^2 (\Delta B_{z,c})$ ($\mu\text{T}/\text{mm}^2$)					
						SL1	SL2	SL3	Avg	Wilcoxon test	
2D	77	86	123	95		2D	19.4	20.2	31.8	23.8	
SMS 3 slices	52	71	79	67	$p = 0.004$	SMS 3 slices	12.4	13.9	20.0	15.4	$p = 0.004$

Note: Loop-Setup (2 mA): Comparison of 2D and SMS-SPARSE approaches in terms of SNR calculated in the MR magnitude images, SDs calculated in the noise floor measurements: $\Delta B_{z,c}$ (measurements without current) in pT, residual $\Delta B_{z,c}$ (measurements with current and after cable correction) in pT, and the Laplacian $\nabla^2 (\Delta B_{z,c})$ in $\mu\text{T}/\text{mm}^2$. Similar to Table 1, each calculation is given as an average across 5 subjects. The Laplacian noise floors $\nabla^2 (\Delta B_{z,c})$ were calculated two-dimensionally in-plane (i.e., neglecting the variations in the slice direction). TES-SETUP (1 mA, A-P): The mean of the SD maps was calculated across three repeated $\Delta B_{z,c}$ and Laplacian $\nabla^2 (\Delta B_{z,c})$ measurements. The reported values are the averages across three different sessions to ensure robustness of the quantitative results (each session has three repeated measurements). All data were first masked with a T_2^* mask. See Table S2 for results calculated in a homogenous white-matter region of interest and for theoretically calculated SDs based on the SNR of the magnitude images. The Wilcoxon signed-rank test was used to test for significance. The results are reported without correction for multiple comparisons.

Abbreviation: SMS, simultaneous multislice; TES, transcranial electrical stimulation.

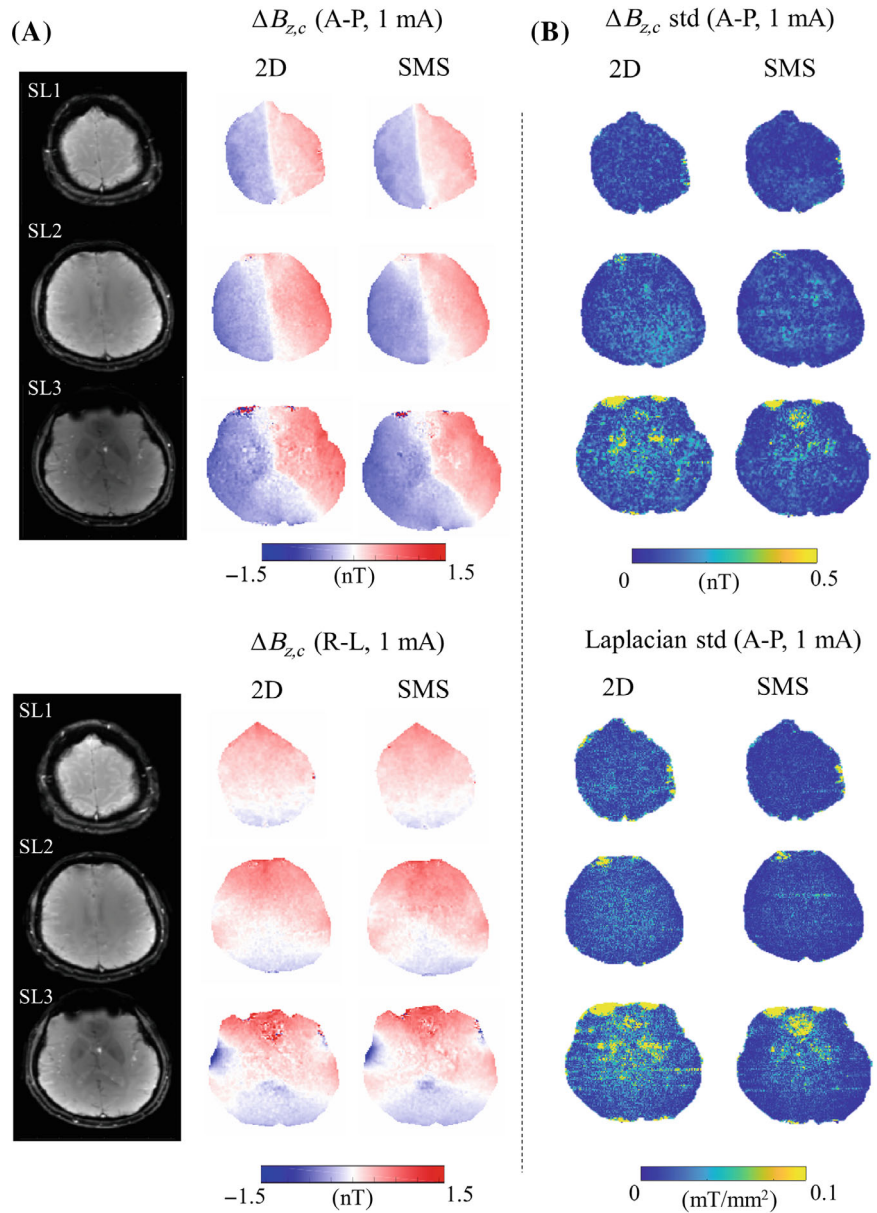
compared with the 2D benchmark. The results of the 4 additional subjects can be found in Figures S6–S9. No severe artifacts are observed in the magnitude images (Figure 3A). Simultaneous acquisition of all three slices performs the best in terms of both $\Delta B_{z,c}$ and Laplacian noise floors (Figure 3B,D; SDs in the upper half of Table 2; 56% and 78% average sensitivity increase against 2D, respectively). The increase in sensitivity is consistent across subjects, and statistically significant ($p < 0.001$). Similar to the residual noise floors in Experiment 1, we observe strategy-independent residual noise floor patterns for the measurements with current flow in the cable loop for some of the subjects (Figure 3C), which suggests that the noise was dominated by imperfect stray field correction. Comparison between the residual noise floors calculated for two different cable paths determined from PETRA scans performed before and after MRCDI demonstrates a significant spatial variation (first vs. second column in Figure 3C). This highlights the importance of minimizing intrascan head and/or cable motion in MRCDI experiments. Interestingly, we observe a subtle horizontal streaking artifact in the Laplacian noise floors for SMS-SPARSE acquisitions, likely due to blood

vessels (Figure 3D; this is most visible in the low-noise background).

3.2.3 | Experiment 3: SMS-SPARSE volume coverage versus 2D benchmark (TES-SETUP)

Results of the first experimental session of Subject 1 are shown in Figure 4. The experiments were repeated in two further sessions, each accommodating three repeated acquisitions for the use in the quantitative analysis (Figure S10 shows the results of the two further sessions). No severe artifacts are observed in the magnitude images. The SMS acquisition significantly and consistently improved the $\Delta B_{z,c}$ image quality and measurement sensitivity for both electrode montages (Figure 4 and lower half of Table 2). Compared with the 2D benchmark, the sensitivity increases by 43% in the $\Delta B_{z,c}$ images and by 55% in the Laplacians (average across the three repeated sessions and three slices). Qualitative assessments of the results for the 3 further subjects confirmed the consistent improvement seen for SMS (Figure S11).

FIGURE 4 Experiment 3. Human in vivo results of MR current density imaging (MRCDI) measurements with simultaneous multislice (SMS) acquisition of three slices, compared with the 2D benchmark for the first subject. (A) Experimental sessions for the electrode montages anterior–posterior (A-P; top) and right–left (R-L; bottom). Each session consists of three repeated acquisitions, and the repetitions are used to calculate mean $\Delta B_{z,c}$ images. Both methods exhibit similar spatial field distributions, whereas SMS provides significantly improved field sensitivity and image quality. (B) Voxel-wise SD maps derived from the three repeated acquisitions in the A-P session for the $\Delta B_{z,c}$ measurements (top) and their Laplacians (bottom). SMS clearly improves the noise floors compared with its 2D counterpart.



3.3 | Reconstruction of current density images

Results for the estimated current density images for the 4 subjects with the A-P electrode montage from Experiment 3 are presented in Figure 5. As an example, Figure 5A,C shows the reference current density and current density error maps for the subject in whom the estimations based on a single SMS acquisition performed worst. Please note that this is a very conservative choice that favors the results obtained for single-slice data. However, even in this case, the results for SMS are only marginally worse than those of the *best case* obtained for single-slice data ($\Delta J = 19.1\%$ vs. 14.3%) and are better in all other cases. The box plot in Figure 5B shows the group data for the current density errors after conductivity

optimization using three slices (obtained with SMS acquisitions) and a single slice (from the standard 2D measurements), respectively. A statistically significant difference ($p < 0.01$) was found, confirming the advantage of current density reconstructions based on SMS compared with single-slice data.

4 | DISCUSSION

We tested two extensions of our previous single-slice 2D-MRCDI approach⁴² to increase spatial coverage, using either a densely sampled volume (3D-DENSE) or sparsely placed simultaneously acquired slices (SMS-SPARSE). While both approaches resulted in clear sensitivity improvements compared with time-matched sequential

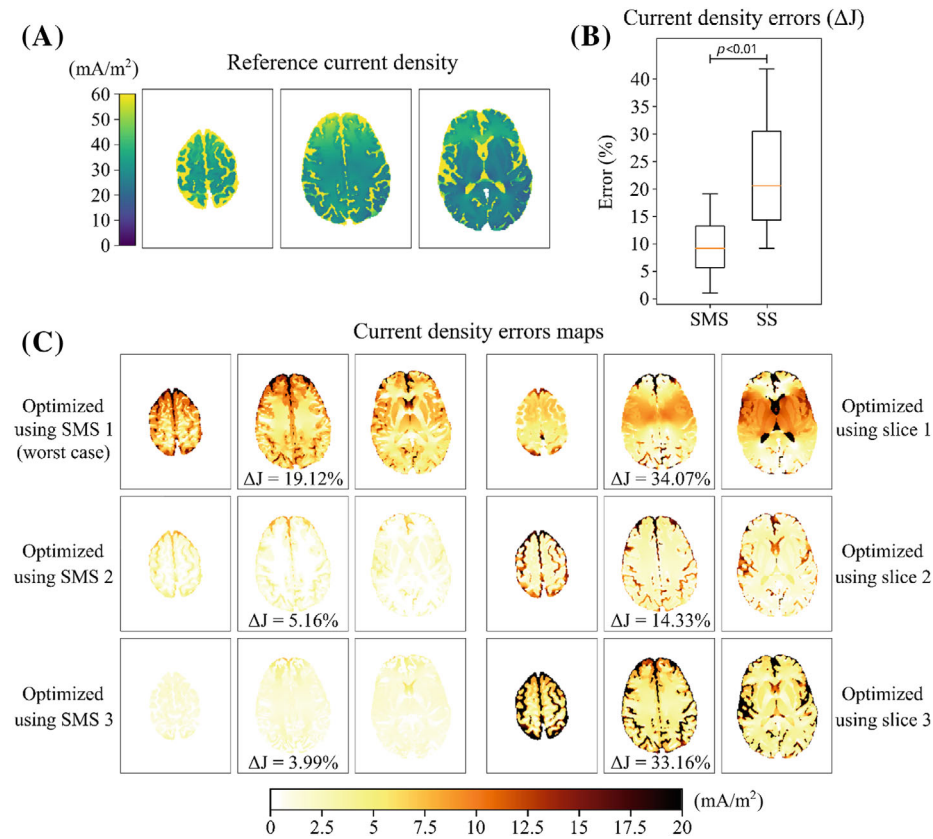


FIGURE 5 Current density error (ΔJ) after performing conductivity optimization based on the three single-slice (SS) measurements and three time-matched simultaneous multislice (SMS) measurements. The 4 subjects from Experiment 3 were used with the anterior–posterior (A-P) electrode montage. (B) Box and whisker plot of ΔJ for all 4 subjects showing a statistically significant difference ($p < 0.01$) for ΔJ when conductivity optimization is based on SMS compared with a single-slice acquisition. The box indicates the interquartile range and the orange line is the median. The whiskers show the minimum and maximum values. (A,C) Reference current density (A) and current density error maps (C) for the subject with the worst-case SMS conductivity optimization. Even in this worst case, conductivity optimization overall works better when three slices are used for optimization.

2D acquisitions in initial phantom experiments, improved sensitivity was primarily maintained for SMS-SPARSE when performing in vivo measurements.

The SMS-SPARSE approach provided a significant sensitivity improvement in $\Delta B_{z,c}$ measurements. This will be very useful for assessing and comparing the quality of different head modeling approaches and for methods that aim to fit the conductivities of the tissue compartments to improve the correspondence between modeled and measured fields.³⁸ Along with improved sensitivity, the SDs of the first-order and second-order spatial derivatives of the measured $\Delta B_{z,c}$ also improved, as demonstrated in the Laplacian noise floors. This can benefit conductivity mapping approaches that are based on the derivatives as input.^{10,13,14,30}

Although the 3D-DENSE approach demonstrated an expected SNR increase and improved $\Delta B_{z,c}$ images in phantoms, this did not translate to human in vivo measurements. Interestingly, the SDs in the Laplacian noise floors were lower compared with the 2D benchmark method. The dense coverage also opens the possibility to calculate gradients of $\Delta B_{z,c}$ images along all three spatial directions. Both features might help to establish derivative-based conductivity mapping approaches for in vivo human brain MREIT,^{10,13,14,30} if the sensitivity of the measurements can be further improved.

Both 3D-DENSE and SMS-SPARSE provide more comprehensive $\Delta B_{z,c}$ information compared with 2D approaches and can therefore improve the accuracy of conductivity mapping or estimation methods. Densely sampled volume measurements mostly provide information on local field variations, whereas sparsely sampled measurements are informative on a broader spatial scale. The accuracy of current density and ohmic conductivity reconstructions from $\Delta B_{z,c}$ information depends on the SNR and the spatial coverage of the $\Delta B_{z,c}$ measurements, and a trade-off between these two properties will often be required to maintain a practically feasible acquisition time. For example, our results show that methods that optimize the ohmic tissue conductivities of head models to improve the fit between modeled and measured fields³⁸ work more stably when the spatial coverage is increased at the cost of lower SNR of the single slices. The best trade-off will be specific for the chosen reconstruction method and will have to be reestablished for other methods to find the most appropriate measurement strategy. Because the sensitivity and image-quality improvements reported for the suggested SMS-SPARSE approach clearly outperforms all other tested techniques, it has the highest potential for future MRCDI studies.

The achieved SDs in the noise floors of the control experiments without current flow are significantly lower than the residual noise floors in some of the experiments

with cable currents. Interestingly, residual noise floors in some of the subjects have similar spatial patterns independent of the used technique, consistent with imperfect correction of the stray magnetic fields caused by the cable currents. In addition, the observed differences between the residual noise floors calculated for two different delineated cable paths based on PETRA acquired before and after MRCDI (1-h intervals) highlights the importance of minimizing both head and cable movement for obtaining reliable results.

4.1 | Future perspectives for MRCDI

The SMS-SPARSE approach allows the measurements of three distant slices with a 78-pT sensitivity to the tiny TES-induced magnetic fields in less than 10 min of total scan time. It demonstrates a clear image-quality improvement in both the measured TES-induced magnetic fields and their derivatives compared with the previously used approaches. We anticipate that these improvements will be useful as a basis for estimating head tissue conductivities, which is needed for generating more realistic individualized head models for TES simulations.³⁸

Our study also shows the stray magnetic fields to be the strongest remaining noise source, most likely caused by intrascan movements of the subject or cables. There is a need to improve the stability and accuracy of the correction methods.

The Laplacian noise floors achieved in this study might also help to establish $\Delta B_{z,c}$ -derivative-based conductivity reconstruction methods^{27,56} in the future. Despite the low SDs achieved in the noise floor images, the Laplacian measurements with current injection did not reveal any obvious current-related spatial patterns (data not shown). However, more advanced filtering approaches might be able to mitigate the still insufficient SNR of the Laplacian images,⁵⁷ but their testing was outside the scope of this study.

As a final note, whether the most effective method for TES current flow and conductivity estimation is based on the direct $\Delta B_{z,c}$ measurements, on their derivatives, or whether a hybrid approach is optimal, is still unknown. Studies focusing on further improvements of reconstruction and fitting strategies are needed.

5 | CONCLUSIONS

Our volumetric approaches, particularly the approach based on simultaneously and sparsely sampled 2D slices, clearly outperformed the standard 2D MRCDI approach by allowing better spatial coverage without compromising

sensitivity. High-quality current-induced field measurements at good resolution in human brains in vivo demonstrated the potential of the improved acquisition methods for future use in studies that aim to estimate the current flow in the brain or the ohmic tissue conductivities of the head. Combined with an efficient conductivity fitting method, they may guide the optimization of TES dosing and help clinical translation.

ACKNOWLEDGMENTS

The financial support of the Lundbeck Foundation (grant no. R288-2018-236 to CG, R324-2019-1784 to LGH, and R244-2017-196 and R313-2019-622 to AT), the Max Planck Society, and the German Research Foundation (Reinhart Koselleck Project, DFG SCHE 658/12) is gratefully acknowledged. Hartwig R. Siebner holds a 5-year professorship in precision medicine at the Faculty of Health Sciences and Medicine, University of Copenhagen, which is sponsored by the Lundbeck Foundation (grant no. R186-2015-2138).


CONFLICT OF INTEREST

Hartwig R. Siebner has received honoraria as speaker from Lundbeck AS (Denmark), Sanofi Genzyme (Denmark), and Novartis (Denmark), as consultant from Lundbeck AS (Denmark), Sanofi Genzyme (Denmark) and as editor-in-chief (NeuroImage Clinical) and senior editor (NeuroImage) from Elsevier Publishers (Amsterdam, The Netherlands). He has received royalties as book editor from Springer Publishers (Stuttgart, Germany) and Gyldendal (Copenhagen, Denmark).

ORCID

Fróði Gregersen  <https://orcid.org/0000-0002-0648-8399>

Klaus Scheffler  <https://orcid.org/0000-0001-6316-8773>

Hasan H. Eroğlu  <https://orcid.org/0000-0002-8723-5894>

Rahel Heule  <https://orcid.org/0000-0002-4589-6483>

Lars G. Hanson  <https://orcid.org/0000-0002-8204-6912>

Axel Thielscher  <https://orcid.org/0000-0002-4752-5854>

REFERENCES

- Bennabi D, Haffen E. Transcranial direct current stimulation (tDCS): a promising treatment for major depressive disorder? *Brain Sci.* 2018;8:81. doi:10.3390/brainsci8050081
- Nitsche MA, Boggio PS, Fregni F, Pascual-Leone A. Treatment of depression with transcranial direct current stimulation (tDCS): a review. *Exp Neurol.* 2009;219:14-19. doi:10.1016/j.expneurol.2009.03.038
- Puonti O, Van Leemput K, Saturnino G, Siebner H, Madsen K, Thielscher A. Accurate and robust whole-head segmentation from magnetic resonance images for individualized head modeling. *Neuroimage.* 2020;219:117044.

4. Thielscher A, Antunes A, Saturnino GB. Field modeling for transcranial magnetic stimulation: a useful tool to understand the physiological effects of TMS? *2015 37th Annual International Conference of the IEEE Engineering in Medicine and Biology Society (EMBC), Milan, Italy.* 2015;222-225. doi:10.1109/EMBC.2015.7318340
5. Joy MLG. MR current density and conductivity imaging: the state of the art. In: *Proceedings of the 26th Annual International Conference of the IEEE Engineering in Medicine and Biology Society*, San Francisco, California, UA. 2004;5315-5319. doi:10.1109/IEMBS.2004.1404484
6. Scott GC, Joy MLG, Armstrong RL, Henkelman RM. Measurement of nonuniform current density by magnetic resonance. *IEEE Trans Med Imaging.* 1991;10:362-374. doi:10.1109/42.97586
7. Scott GC, Joy MLG, Armstrong RL, Henkelman RM. Sensitivity of magnetic-resonance current-density imaging. *J Magn Reson.* 1992;97:235-254.
8. Eyüboğlu BM, Reddy R, Leigh JS. Imaging electrical current density using nuclear magnetic resonance. *Turk J Elec Eng Comp Sci.* 1998;6:201-214.
9. Eyüboğlu BM. Magnetic resonance-electrical impedance tomography. *Encyclopedia of Biomedical Engineering.* Vol 4. Wiley; 2006:2154-2162.
10. Eyüboğlu BM. Magnetic resonance current density imaging. In: *Metin Akay, ed. Encyclopedia of Biomedical Engineering.* Hoboken, New Jersey, USA: Wiley. 2006;4:2147-2153.
11. Seo JK, Woo EJ. Electrical tissue property imaging at low frequency using MREIT. *IEEE Trans Biomed Eng.* 2014;61:1390-1399. doi:10.1109/TBME.2014.2298859
12. Oh SH, Lee BI, Park TS, et al. Magnetic resonance electrical impedance tomography at 3 Tesla field strength. *Magn Reson Med.* 2004;51:1292-2196. doi:10.1002/mrm.20091
13. Seo JK, Woo EJ. Magnetic resonance electrical impedance tomography. *Soc Ind Appl Math.* 2011;53:40-68.
14. Seo JK, Kwon O, Woo EJ. Magnetic resonance electrical impedance tomography (MREIT): conductivity and current density imaging. *J Phys Conf Ser.* 2005;12:140-155. doi:10.1088/1742-6596/12/1/014
15. Sadighi M, Şişman M, Açıkgöz BC, Eroğlu HH, Eyüboğlu BM. Low-frequency conductivity tensor imaging with a single current injection using DT-MREIT. *Phys Med Biol.* 2021;66:66. doi:10.1088/1361-6560/abddcf
16. Song Y, Sajib SZK, Wang H, et al. Low frequency conductivity reconstruction based on a single current injection via MREIT. *Phys Med Biol.* 2020;65:225016. doi:10.1088/1361-6560/abbc4d
17. Jeong WC, Kim YT, Minhas AS, et al. In vivo conductivity imaging of human knee using 3 mA injection current in MREIT. *J Phys Conf Ser.* 2010;224:012148. doi:10.1088/1742-6596/224/1/012148
18. Jeon K, Minhas AS, Kim YT, et al. MREIT conductivity imaging of the postmortem canine abdomen using CoReHA. *Physiol Meas.* 2009;30:957-966.
19. Meng Z, Sajib SZ, Chauhan M, et al. Improved conductivity image of human lower extremity using MREIT with chemical shift artifact correction. *Biomed Eng Lett.* 2012;2:62-68. doi:10.1007/s13534-012-0052-0
20. Han YQ, Meng ZJ, Jeong WC, et al. MREIT conductivity imaging of canine head using multi-echo pulse sequence. *J Phys Conf Ser.* 2010;224:012078. doi:10.1088/1742-6596/224/1/012078
21. Jeong WC, Sajib SZK, Katoch N, Kim HJ, Kwon OI, Woo EJ. Anisotropic conductivity tensor imaging of in vivo canine brain using DT-MREIT. *IEEE Trans Med Imaging.* 2017;36:124-131. doi:10.1109/TMI.2016.2598546
22. Kim HJ, Oh TI, Kim YT, et al. In vivo electrical conductivity imaging of a canine brain using a 3 T MREIT system. *Physiol Meas.* 2008;29:1145-1155. doi:10.1088/0967-3334/29/10/001
23. Kim HJ, Jeong WC, Kim YT, et al. In vivo conductivity imaging of canine male pelvis using a 3 T MREIT system. *J Phys Conf Ser.* 2010;224:012020. doi:10.1088/1742-6596/224/1/012020
24. Birgül Ö, Eyüboğlu BM, Ider YZ. Experimental results for 2D magnetic resonance electrical impedance tomography (MR-EIT) using magnetic flux density in one direction. *Phys Med Biol.* 2003;48:3485-3504.
25. Sadighi M, Göksu C, Eyüboğlu BM. J-based magnetic resonance conductivity tensor imaging (MRCTI) at 3 T. *Proceedings of the 36th Annual International Conference of the IEEE Engineering in Medicine and Biology Society*, Chicago, Illinois, USA 2014 1139-1142.
26. Ider YZ, Birgül Ö. Use of the magnetic field generated by the internal distribution of injected currents for electrical impedance tomography (MR-EIT). *Turk J Elec Eng Comp Sci.* 1998;6:215-225.
27. Oh SH, Il LB, Woo EJ, et al. Conductivity and current density image reconstruction using harmonic Bz algorithm in magnetic resonance electrical impedance tomography. *Phys Med Biol.* 2003;48:3101-3116. doi:10.1088/0031-9155/48/19/001
28. Oh SH, Lee BI, Woo EJ, et al. Electrical conductivity images of biological tissue phantoms in MREIT. *Physiol Meas.* 2005;26:S279-S288. doi:10.1088/0967-3334/26/2/026
29. Sadleir R, Zhang S, Grant S, et al. Noise analysis of MREIT at 3 T and 11 T field strength. *Proceedings of the 27th Annual International Conference of the IEEE Engineering in Medicine and Biology Society*, Shanghai, China. 2005;3:2637-2640. doi:10.1109/IEMBS.2005.1617011
30. Woo EJ, Seo JK. Magnetic resonance electrical impedance tomography (MREIT) for high-resolution conductivity imaging. *Physiol Meas.* 2008;29:R1-R26. doi:10.1088/0967-3334/29/10/R01
31. Minhas AS, Jeong WC, Kim YT, Han Y, Kim HJ, Woo EJ. Experimental performance evaluation of multi-echo ICNE pulse sequence in magnetic resonance electrical impedance tomography. *Magn Reson Med.* 2011;66:957-965. doi:10.1002/mrm.22872
32. Göksu C, Hanson LG, Siebner HR, Ehses P, Scheffler K, Thielscher A. Human in-vivo brain magnetic resonance current density imaging (MRCDI). *Neuroimage.* 2018;171:26-39. doi:10.1016/j.neuroimage.2017.12.075
33. Chauhan M, Indahlastari A, Kasinadhuni AK, Schar M, Mareci TH, Sadleir RJ. Low-frequency conductivity tensor imaging of the human head in vivo using DT-MREIT: first study. *IEEE Trans Med Imaging.* 2018;37:966-976. doi:10.1109/TMI.2017.2783348
34. Kasinadhuni AK, Indahlastari A, Chauhan M, Schär M, Mareci TH, Sadleir RJ. Imaging of current flow in the human head during transcranial electrical therapy. *Brain Stimul.* 2017;10:764-772. doi:10.1016/j.brs.2017.04.125
35. Jog MV, Smith RX, Jann K, et al. In-vivo imaging of magnetic fields induced by transcranial direct current stimulation (tDCS) in human brain using MRI. *Sci Rep.* 2016;6:34385. doi:10.1038/srep34385

36. Sajib SZ, Chauhan M, Kwon OI, Sadleir RJ. Magnetic-resonance-based measurement of electromagnetic fields and conductivity in vivo using single current administration—a machine learning approach. *PLoS One*. 2021;16:e0254690. doi:10.1371/journal.pone.0254690
37. Antal A, Alekseichuk I, Bikson M, et al. Low intensity transcranial electric stimulation: safety, ethical, legal regulatory and application guidelines. *Clin Neurophysiol*. 2017;128:1774-1809. doi:10.1016/j.clinph.2017.06.001
38. Eroglu HH, Puonti O, Göksu C, et al. On the reconstruction of magnetic resonance current density images of the human brain: pitfalls and perspectives. *Neuroimage*. 2021;243:118517. doi:10.1016/j.neuroimage.2021.118517
39. Göksu C, Scheffler K, Ehses P, Hanson LG, Thielscher A. Sensitivity analysis of magnetic field measurements for magnetic resonance electrical impedance tomography (MREIT). *Magn Reson Med*. 2017;79:748-760. doi:10.1002/mrm.26727
40. Gregersen F, Göksu C, Schaefers G, Xue R, Thielscher A, Hanson LG. Safety evaluation of a new setup for transcranial electric stimulation during magnetic resonance imaging. *Brain Stimul*. 2021;14:488-497. doi:10.1016/j.brs.2021.02.019
41. Göksu C, Scheffler K, Siebner HR, Thielscher A, Hanson LG. The stray magnetic fields in magnetic resonance current density imaging (MRCDI). *Phys Med*. 2019;59:142-150. doi:10.1016/j.ejmp.2019.02.022
42. Göksu C, Heule R, Scheffler K, et al. Sensitivity and resolution improvement for in vivo magnetic resonance current—density imaging of the human brain. *Magn Reson Med*. 2021;86:3131-3146. doi:10.1002/mrm.28944
43. Bernstein MA, King KF, Zhou XJ. *Handbook of MRI Pulse Sequences*. Elsevier Academic Press; 2004.
44. Nam HS, Kwon OI. Optimization of multiply acquired magnetic flux density $B(z)$ using ICNE-multiecho train in MREIT. *Phys Med Biol*. 2010;55:2743-2759. doi:10.1088/0031-9155/55/9/021
45. Breuer FA, Blaimer M, Heidemann RM, Mueller MF, Griswold MA, Jakob PM. Controlled aliasing in parallel imaging results in higher acceleration (CAIPIRINHA) for multi-slice imaging. *Magn Reson Med*. 2005;53:684-691. doi:10.1002/mrm.20401
46. Pruessmann KP, Weiger M, Scheidegger MB, Boesiger P. SENSE: sensitivity encoding for fast MRI. *Magn Reson Med*. 1999;42:952-962.
47. Tikhonov AN. Regularization of incorrectly posed problems. *Sov Math Dokl*. 1963;4:1624-1627.
48. Walsh DO, Gmitro AF, Marcellin MW. Adaptive reconstruction of phased array MR imagery. *Magn Reson Med*. 2000;43:682-690.
49. Pohmann R, von Kienlin M. Accurate phosphorus metabolite images of the human heart by 3D acquisition-weighted CSI. *Magn Reson Med*. 2001;45:817-826. doi:10.1002/mrm.1110
50. Budde J, Shajan G, Scheffler K, Pohmann R. Ultra-high resolution imaging of the human brain using acquisition-weighted imaging at 9.4T. *Neuroimage*. 2014;86:592-598. doi:10.1016/j.neuroimage.2013.08.013
51. Pohmann R, Ugurbil K. Acquisition-weighted CSI with a small number of scans. *Proceedings of the 15th Joint Annual Meeting of ISMRM-ESMRMB*, Berlin, Germany 2007 1236.
52. Heule R, Celicanin Z, Kozerke S, Bieri O. Simultaneous multislice triple-echo steady-state (SMS-TESS) T1, T2, PD, and off-resonance mapping in the human brain. *Magn Reson Med*. 2018;80:1088-1100. doi:10.1002/mrm.27126
53. Barth M, Breuer F, Koopmans PJ, Norris DG, Poser BA. Simultaneous multislice (SMS) imaging techniques. *Magn Reson Med*. 2016;75:63-81. doi:10.1002/mrm.25897
54. Banan G, Chauhan M, Amin M, et al. *Phase dispersion from steady-state signal behavior in phase-sensitive multiband imaging with application to MREIT*. *Proceedings of the Annual Meeting of ISMRM [Virtual]*; 2021:3787.
55. Ida M, Wakayama T, Nielsen ML, Abe T, Grodzki DM. Quiet T1-weighted imaging using PETRA: initial clinical evaluation in intracranial tumor patients. *J Magn Reson Imaging*. 2015;41:447-453. doi:10.1002/jmri.24575
56. Seo JK, Yoon J, Woo EJ, Kwon O. Reconstruction of conductivity and current density images using only one component of magnetic field measurements. *IEEE Trans Biomed Eng*. 2003;50:1121-1124.
57. Lee CO, Jeon K, Ahn S, Kim HJ, Woo EJ. Ramp-preserving denoising for conductivity image reconstruction in magnetic resonance electrical impedance tomography. *IEEE Trans Biomed Eng*. 2011;58:2038-2050. doi:10.1109/TBME.2011.2136434

SUPPORTING INFORMATION

Additional supporting information may be found in the online version of the article at the publisher's website.

Figure S1. Schematic diagram of a spoiled gradient-echo MR current density imaging (MRCDI) sequence (see Section 2 and Refs. 1–3 for details).

Figure S2. Experiment 1. Human in vivo experiments of the second subject for comparison of the 3D-DENSE approach against 2D.

Figure S3. Experiment 1. The third subject for comparison of the 3D-DENSE approach against 2D.

Figure S4. Experiment 1. The fourth subject for comparison of the 3D-DENSE approach against 2D.

Figure S5. Experiment 1. The fifth subject for comparison of 3D-DENSE approach against 2D.

Figure S6. Experiment 2. Human in vivo experiments of the second subject for comparison of the simultaneous multislice (SMS)–SPARSE approach against 2D.

Figure S7. Experiment 2. The third subject for comparison of the SMS-SPARSE approach against 2D.

Figure S8. Experiment 2. The fourth subject for comparison of the SMS-SPARSE approach against 2D.

Figure S9. Experiment 2. The fifth subject for comparison of the SMS-SPARSE approach against 2D.

Figure S10. Experiment 3. Human in vivo results of the MR current density imaging (MRCDI) measurements with the best-performing simultaneous multislice (SMS)–SPARSE technique against the 2D benchmark for the first subject.

Figure S11. Experiment 3. Human in vivo results of the MR current density imaging (MRCDI) measurements with the best-performing simultaneous multislice

(SMS)–SPARSE technique against 2D benchmark for Subjects 2–4 and an anterior–posterior electrode montage (1 mA).

Figure S12. Experiment S1-a: The 2D and simultaneous multislice (SMS)–2SL measurements of a volume consisting of sparsely distributed slices.

Figure S13. Experiment S1-b: Limitations of using a high number of slices for the simultaneous multislice (SMS)–SPARSE technique.

Figure S14. Experiment S2: The 2D and volumetric approaches to measure a volume consisting of densely distributed slices.

Table S1. Experiment S1-a: The 2D and simultaneous multislice (SMS)–2SL measurements of a volume consisting of sparsely distributed slices.

Table S2. Experiment S2: The 2D versus 3D-DENSE approaches.

How to cite this article: Göksu C, Gregersen F, Scheffler K, et al. Volumetric measurements of weak current–induced magnetic fields in the human brain at high resolution. *Magn Reson Med.* 2023;90:1874–1888. doi: 10.1002/mrm.29780